Photo- and radio-luminescence of porphyrin functionalized ZnO/SiO_2 nanoparticles

Roberta Crapanzano[a], **Irene Villa***[b], **Silvia Mostoni**[ac], **Massimiliano D'Arienzo**[ac], **Barbara Di Credico**[ac], **Mauro Fasoli**[a], **Roberto Lorenzi**[a], **Roberto Scotti**[ac] **and Anna Vedda**[a]

[a]*Department of Materials Science, University of Milano – Bicocca, Via Cozzi 55, I-20125, Milano, Italy*

[b]*Institute of Physics of the Czech Academy of Sciences (FZU), Cukrovarnická 10/112, 162 00 Prague, Czech Republic. E-mail: villa@fzu.cz*

[c]*INSTM, University of Milano – Bicocca, Via Cozzi 55, I-20125, Milano, Italy*

Abstract

The development of hybrid nanoscintillators is hunted for the implementation of modern detection technologies, like in high energy physics, homeland security, radioactive gas sensing, and medical imaging, as well as of the established therapies in radiation oncology, such as in X-ray activated photodynamic therapy. Engineering of the physico-chemical properties of nanoparticles (NPs) enables the manufacture of hybrids in which the conjugation of inorganic/organic components leads to increased multifunctionality and performance. However, the optimization of the properties of nanoparticles in combination with the use of ionizing radiation is not trivial: a complete knowledge on the structure, composition, physico-chemical features, and scintillation property relationships in hybrid nanomaterials is pivotal for any applications exploiting X-rays. In this paper, the design of hybrid nanoscintillators based on ZnO grown onto porous SiO_2 substrates (ZnO/SiO_2) has been performed in the view to create nanosystems potentially suitable in X-ray activated photodynamic therapy. Indeed, cytotoxic porphyrin dyes with increasing concentrations have been anchored on ZnO/SiO_2 nanoparticles through amino-silane moieties. Chemical and structural analyses correlated with photoluminescence reveal that radiative energy transfer between ZnO and porphyrins is the principal mechanism prompting the excitation of photosensitizers. The use of soft X-ray excitation results in a further sensitization of the porphyrin emission, due to augmented energy deposition promoted by ZnO in the surroundings of the chemically bound porphyrin. This finding unveils the cruciality of the design of hybrid nanoparticles in ruling the efficacy of the interaction between ionizing radiation and inorganic/organic moieties, and thus of the final nanomaterial performances towards the foreseen application.

Introduction

Organic and inorganic NPs as large as 1 to 100 nm are exploited in a wide range of applications,[1–3] such as in scintillation and lighting, electronics, catalysis, surface coating, cosmetics, and biomedicine.[2–4] They present unique physico-chemical qualities that can be controlled by the composition, size, shape, and structure, as well as the stability and ease of functionalization.[5,6] Besides, the high surface area and reactivity of NPs enable the loading with various functional groups, hydrophobic molecules, organic dyes, DNA moieties, and polymers that improve their colloidal dispersibility, stability and surface electronic properties for specific applications.[7–10] The development of advanced synthesis methods has allowed the creation of a class of novel hybrid nanomaterials, consisting of diverse targeted organic moieties, whose qualities surpass those of the parent components and can be described as a synergetic combination of the properties of the constituents.[11] The class of hybrid NPs meets the interest of biomedical technologies for biosensing, imaging, and radiation oncology therapy applications.[12] One of the promising oncological therapies for the treatment of deep tumours is X-ray activated photodynamic therapy (X-PDT),[13] based on the simultaneous application of radiotherapy and photodynamic therapy (PDT). The strategy relies on the exploitation of hybrid NPs featuring dense and high atomic number (*Z*) scintillating nanoparticles converting ionizing radiations into ultraviolet light or visible light; in addition, the surface of the dense NP is typically grafted with organic dyes as cytotoxic photosensitizers (PSs), able to generate reactive oxygen species (ROS), especially singlet oxygen moieties, upon excitation.[14,15] The X-ray excited NP can trigger the cancer killing actions of the PS on the surface through multiple radiative emission and reabsorption process, as well as through efficient energy transfer mechanisms (ET).[16,18,19]

The current literature proposes an extensive investigation on nanomaterials suitable for X-PDT – such as oxides, fluorides, silica-based nanostructures, and semiconductor nanocrystals combined with organic PSs – with proofs of the higher efficacy of X-PDT in killing tumour cells with respect to the traditional individual radiotherapy and PDT.[15,19–21] The recent experimental results have assessed that the outstanding qualities of the hybrid NP enable the performance of the modern technology to be improved in diverse areas, particularly regarding the advancement in X-ray based diagnostic and therapeutic tools.[22–24] Despite the evidence, the achievement of an exhaustive knowledge of the physical processes involving the interaction of the ionizing radiation and the energy deposition mechanism within hybrid systems at the nanoscale is eagerly hunted. In hybrids, the high *Z* of the inorganic elements in proximity to the organic molecules allows in enhancing the interaction cross section of the nanohybrid with ionizing radiations,[17] leading to NP excitation and the release of many secondary free carriers in the surrounding that, afterwards, interact with the coupled PS. However, computational analyses have shown that the reduced material dimension is critical in the presence of high energy ionizing radiation, since the nanometric size is much smaller than the secondary carrier mean free path generated within the material by the first ionizing event.[25] A significant fraction of the X-ray energy is lost outside the NP, supposedly limiting the applicability of the hybrid nanoscintillators.[26,27] Thus, the architecture of the nanohybrids and the type of dense nanoscintillators and organic dyes with appropriate physico-chemical properties, together with the

selection of surface functionalization strategies, in terms of the dye concentration and spatial distribution on the NP surface, are key points for the development of high performance materials.

To provide a complete description of the relationship among nanoscintillator, PS, and ionizing radiation with respect to the final performance of the nanohybrids, we have performed the synthesis and structural and spectroscopic analyses on a model system of porphyrin functionalized zinc oxide NPs, which can also be considered for X-PDT purposes due to the high ability of porphyrin to generate singlet oxygen species.[28] In particular, ZnO NPs with a diameter of 4–6 nm were grown directly on highly porous SiO_2 spherical particle substrates (ZnO/SiO_2) and then functionalized with different amounts of meso-tetra(4-carboxyphenyl)porphyrin (TCPP) anchored to the silica surfaces through amino-silane groups. Among nanomaterials, ZnO NPs have been proposed for medical applications due to their low toxicity and good anti-cancer and anti-microbial activities.[29] Silica coated ZnO NPs have been studied as radiosensitizers to enhance the radiotherapy cytotoxic effects.[30] Moreover, ZnO NPs conjugated with porphyrin derivatives have been proposed as agents in PDT and X-PDT.[31–33] Indeed, ZnO is a wide band gap (~3.4 eV) semiconductor with a large excitonic binding energy (~60 meV),[34] and it displays a near-UV excitonic emission accompanied by several visible defect-related bands under X-rays (radioluminescence – RL) and light (photoluminescence – PL) excitations.[34–37] Thus, ZnO visible emissions enable in efficiently stimulating diverse organic PSs, especially porphyrins, with the subsequent generation of cytotoxic species, since the PS typical absorption spans in the visible spectral range from the violet to the orange region.[38] The occurrence of radiative and non-radiative ET mechanisms from the NP to the PS in nanohybrids is guaranteed by the overlap between the NP luminescence emission and the PS absorption features.[14,19,39]

In this work, we have highlighted that, under X-ray irradiation, the ET mechanisms are not trivial, since, beside the excitation of the porphyrin moiety by ZnO, the direct interaction of the ionizing radiation with the TCPP and energy deposition in the surroundings of the NP must be considered as factors affecting the trigger of the cancer killing mechanism and the therapeutic outcome of the hybrid ZnO.[20] For this investigation, the luminescence properties of the TCPP functionalized and bare ZnO/SiO_2 nanoscintillators and the TCPP molecules alone have been detected under both light and X-ray excitation. In particular, we have explored the ET probability and the energy deposition mechanism as a function of the dye loading level and the intra- and inter-spatial distributions of the ZnO NPs and the porphyrin molecules; these are crucial parameters to avoid the formation of PS aggregates, namely J-aggregates and H-aggregates,[40–42] acting as quenching channels for the PS emission with a detrimental reduction of ROS and singlet oxygen production.[43,44]

This work shows a consistent approach to check the manufacture process of hybrid NPs, based on the exploration of the properties of the individual components and the final hybrid architecture. The validity of the study goes beyond the experimental findings on the specific case of TCPP functionalized ZnO/SiO_2, as it proves the importance of achieving a high-level control of the tuneability of hybrid nanoparticle properties. Indeed, the engineering of the morphological, structural, and luminescence features of the components of hybrid nanosystems and the nanohybrid itself is a fundamental step to create materials with performances that could match with the specific requests of the advanced X-ray-based applications and techniques.

Results and discussion

Morphological and structural characterization

Porphyrin functionalized ZnO/SiO_2 systems were prepared following a four-step procedure as shown in Fig. 1. Briefly, ZnO NPs were previously anchored onto the porous SiO_2 substrate (ZS, steps I and II); then, amino-silane (3-aminopropyltriethoxysilane, APTES) was attached to the SiO_2 surface (ZS-A, step III) and TCPP molecules were covalently bonded to them (ZS-A-PY, step IV, where Y is the APTES : TCPP molar ratios, equal to 1 : 1, 1 : 0.5, 1 : 0.25, and 1 : 0.1). All the operative details are reported in the Experimental Section.

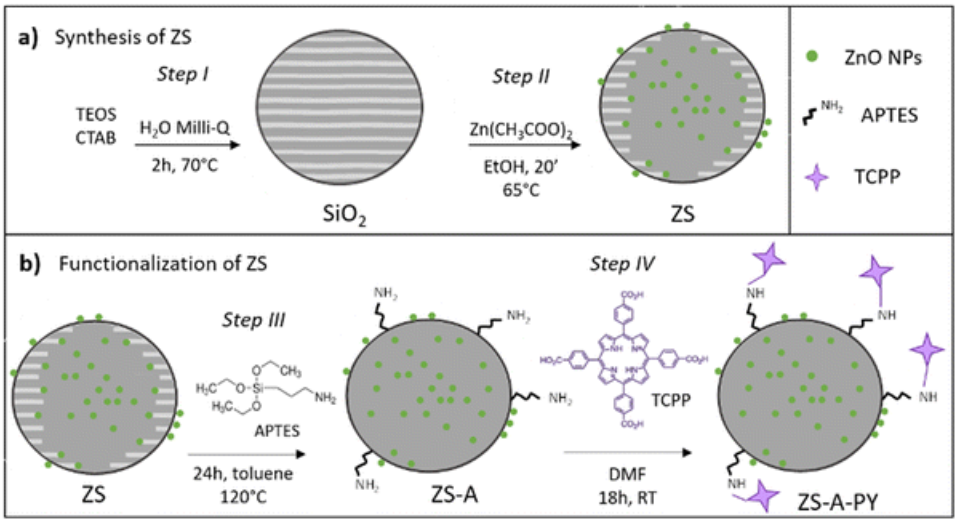

Fig. 1 *Reaction paths for the synthesis of ZS-AP-Y: (a) synthesis of ZS (steps I and II) and (b) functionalization of ZS (steps III and IV). For each step, a schematic representation of the morphological features is reported.*

First, the morphology of all samples was investigated by transmission electron microscopy (TEM) analysis. TEM images of SiO_2 (Fig. 2(a) and (b)) confirmed the formation of almost spherical SiO_2 NPs, with an average size of 80 ± 6 nm and ordered mesoporous channels of few nanometer diameter (average diameter 3 ± 1 nm), generated by the cetyltrimethylammonium bromide (CTAB) self-assembly during SiO_2 growth.

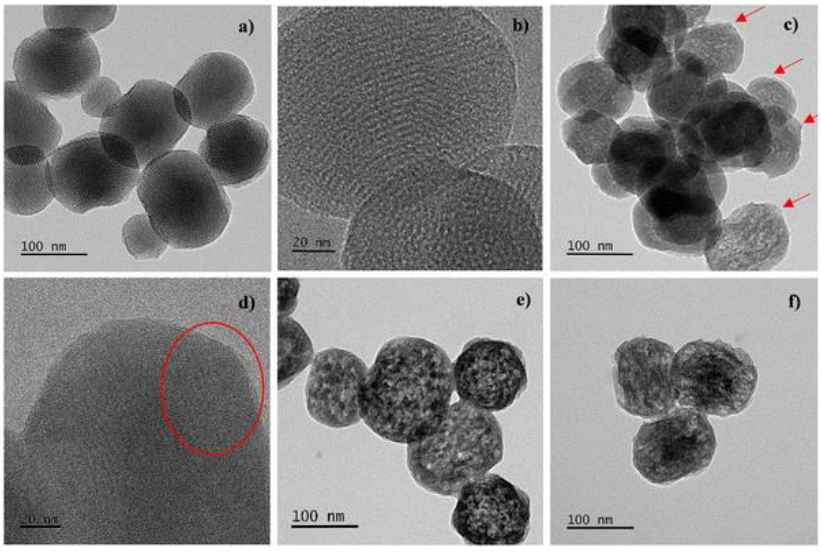

Fig. 2 *TEM images of SiO_2 NPs (a) and (b), ZS (c) and (d), ZS-A (e) and ZS-AP-1 (f) as an example of ZS-AP-Y samples. The red arrows in (c) indicate the ZnO NPs grown on the external SiO_2 surface.*

In step II, the effective formation of ZnO NPs was first validated by diffuse reflectance spectroscopy (DRS) analysis (Fig. S1, ESI†), which showed the absorbance features in ZS corresponding to the typical ZnO band gap energy (~3.2 eV). Besides, the good Zn distribution over the SiO_2 NPs was assessed by elemental mapping (Fig. S2, ESI†). TEM images of ZS show ZnO NPs of 4–6 nm in diameter on the external SiO_2 surface (red arrows, Fig. 2(c)) through the interaction of the zinc precursor in basic ethanol solution with the surface –OH groups of SiO_2. However, ZnO NPs partially grow also in the mesopores of SiO_2 NPs, as schematically depicted in the step II of Fig. 1. In fact, the long-range order of the parallel channels in the pristine SiO_2 almost totally disappeared in ZS, overlapped by the low contrast and darker superimposed images of the ZnO particles in the silica bulk, caused by the presence of the high-atomic number Zn element in the inner part of SiO_2 NPs. Only a residual mesoporosity is detectable in ZS, as evidenced by the red circle in Fig. 2(d).

This observation can be explained considering that, during step II, the solution of the zinc precursor is able to penetrate the mesoporous channels of SiO_2 due to the high available specific surface area (SSA = 1100 $m^2 g^{-1}$) leading to the formation of ZnO NPs inside the SiO_2 mesoporosity. Accordingly, the nitrogen physisorption analysis on ZS showed a severe reduction of a SSA value (109 $m^2 g^{-1}$), and a strong decrease of the cumulative pore volume (DCPV), which can be connected to the almost total disappearance of the SiO_2 mesopores with a size between 1.5 and 3.0 nm (Fig. S3, ESI†). This suggests that the growth of ZnO NPs destroyed the ordered mesoporosity of SiO_2 producing a residual smaller amount of disordered interparticle pores.

After ZS functionalization with APTES, TEM images of ZS-A evidenced a further modification of the SiO_2 morphology. The SiO_2 ordered mesoporosity was not detectable, suggesting that APTES molecules penetrated into the residual available SiO_2 pores (Fig. 2(e)) but condensed mainly on the external SiO_2 surface. The image of the NPs shows high and low contrast spotted areas, ascribed to the presence of higher and lower atomic number elements, Zn and Si, respectively, due to amorphous ZnO NPs grown in the inner part of the amorphous SiO_2, where the ordered mesoporosity was modified by reactions between the silica matrix and both the zinc precursor and APTES. In ZS-AP-Y, these morphological features were not altered by TCPP addition in step IV (Fig. 2(f)), and no detrimental effects on the Zn distribution were detected through the elemental mapping of ZS-AP-Y (Fig. S2, ESI†).

From the structural point of view, X-ray powder Diffraction (XRPD) analysis evidenced the amorphous character of both SiO_2 and ZnO NPs. The only feature in ZS is the broad peak at $2\vartheta = 22°$ due to amorphous SiO_2 (Fig. S4, ESI†) and no other peaks were detectable in ZS-A and ZS-AP-Y, implying that no crystalline structures were formed and no porphyrin aggregation into crystalline domains occurred.[45]

Fourier transform infrared spectroscopy (FTIR) in the attenuated total reflectance (ATR) validated the functionalization. Firstly, in the ATR-FTIR spectrum of ZS compared to SiO_2 (Fig. S5a, ESI†), the absence of the peak at 958 cm^{-1}, attributed to the surface –OH groups of SiO_2, suggested the ZnO anchoring on the SiO_2 surface through their partial replacement with Si–O–Zn

bonds.[46] Moreover, the ZS-A sample compared to ZS (Fig. S5a, ESI†) shows two new peaks at 2930 cm^{-1} and 2860 cm^{-1} assigned to the asymmetric and symmetric stretching of $–CH_2$ groups (ν_{as} and ν_s) of the APTES propyl chains, in agreement with the spectra of pure APTES (Fig. S5b, ESI†). The same peaks were observed in the SiO_2-functionalized sample with higher APTES amount (3.0 wt%, ZS-A-3, Fig. S5b, ESI†), where the higher peak intensity was due to the higher functionalization degree. Besides, the absence of the peaks due to the ethoxy groups confirmed the efficient reaction of APTES with the surface OH groups of SiO_2 through their hydrolysis and condensation. The peaks at 2930 and 2860 cm^{-1} were similarly evident in ZS-AP-Y (Fig. S5a, ESI†), validating the stability of ZS-A in *N,N*-dimethylformamide (DMF), used as the reaction solvent both for the TCPP interaction and for the PL measurements. No strong signals due to TCPP were detected in the ATR-FTIR spectra of ZS-AP-Y because of the very low TCPP amounts used in the synthesis.

Raman spectroscopy was performed to obtain insights into the amorphous nature of both SiO_2 and ZnO as well as their interaction in the ZS sample. The Raman spectrum of bare SiO_2 showed the main vibrational modes expected for Si–O bonds in the amorphous network,[47–50] indicative of a relaxed structure typical for sol–gel derived silica not fully densified (Fig. S6, ESI†).[51–53] Besides, in the spectrum of ZS, a superposition of amorphous SiO_2 and ZnO signals was observed. These signals were compared to the spectra of bare SiO_2 and amorphous ZnO NPs, prepared under the same reaction conditions without adding SiO_2 NPs and used as a reference material. In fact, the two broad bands in the region 300–400 cm^{-1}, the small peak at 440 cm^{-1} (similar to the E_2 mode of ZnO) and the unstructured broad band at 500–800 cm^{-1} due to amorphous-like ZnO,[54,55] along with the typical SiO_2 signals, led to the formation of a plateau region, followed by a shoulder at higher wavenumbers. Moreover, the strong enhancement of the peak at 1100 cm^{-1} assigned to the longitudinal asymmetric stretching (ω_3) of bare SiO_2 can be attributed to the superposition of two-phonon features of longitudinal modes (2LO) which may arise in disordered ZnO.[55] Interestingly, the anchoring of ZnO NPs also led to a strong reduction of the symmetric stretch vibrations of silanol groups (ν = 975 cm^{-1}),[56] confirming the FTIR results and validating that surface OH groups may act as the anchoring site for ZnO.

The amounts of APTES and TCPP linked to SiO_2 were evaluated by the thermogravimetric analysis (TGA) thermal profiles of ZS-A and ZS-AP-Y, by comparing them to bare ZS (Fig. 3). The weight loss $\Delta W_{150–1000\ °C}$ increased from ZS to ZS-A and ZS-AP-Y and the highest values were measured at the highest TCPP amount. The amounts of APTES and TCPP in ZS-AP-Y were calculated from $\Delta W_{150–1000\ °C}$ and are close to the nominal ones (Table S1, ESI†). Besides, the calculated molar ratios between TCPP and APTES over SiO_2 were similar to the expected nominal values (Table S1, ESI†), suggesting that the anchoring of TCPP to SiO_2 was carried out under high controlled conditions. The TGA results were further validated by the elemental CHNS analysis, where the increased N% of ZS-A and ZS-AP-Y compared to bare ZS was assigned to the nitrogen contributions given by both APTES and TCPP molecules. For TGA analysis, the *N*% increased by increasing the TCPP amount and the results were very similar to the nominal values (Table S1, ESI†).

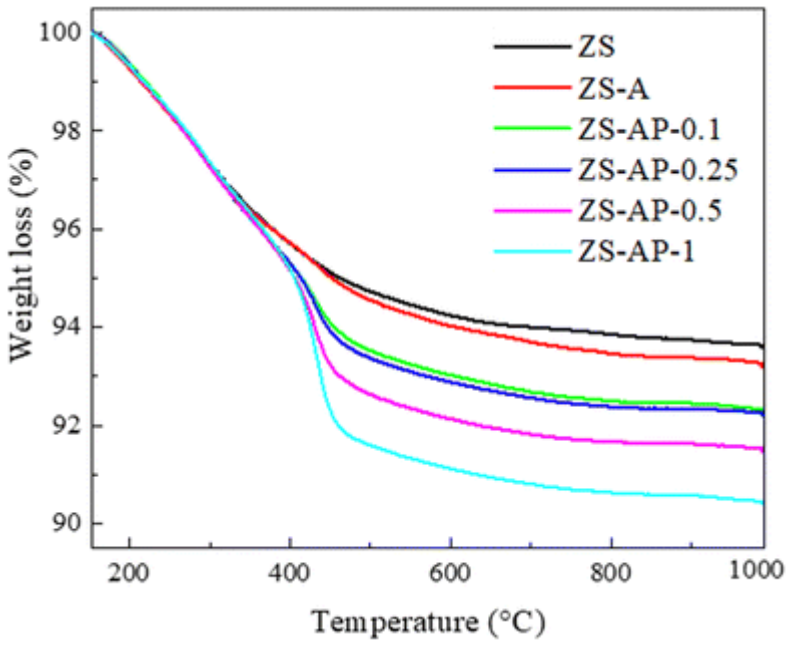

Fig. 3 *TGA profiles in the temperature range of 150–1000 °C for ZS, ZS-A and ZS-AP-Y.*

At last, the absorption spectra of the TCPP alone and ZS-AP-Y dispersed in DMF were obtained to investigate the TCPP absorption features upon anchoring on ZS and estimate its amount in the samples (Fig. S7 and Table S2, ESI†). All the spectra disclose the characteristic porphyrin absorption features: the Soret band at about 3.0 eV (~410 nm) and the Q-bands between 1.8 (~700 nm), and 2.7 eV (~450 nm), related to $S_0 \rightarrow S_2$ and $S_0 \rightarrow S_1$ transitions,[57] respectively. However, the wide Soret band observed in ZS-AP-Y, whose broadening progressively increases with the TCPP concentration, with respect to the sharp peak of the dye alone, unveils the occurrence of dye aggregates and the dependence of their formation probability on the porphyrin content.[42,58] By focusing on the main Q-band at about 2.4 eV (~520 nm), the spectra of ZS-AP-Y show that the absorption scales coherently with the dye content and the estimated TCPP concentrations in the samples (measured at a constant ZnO amount = 10^{-3} M) were consistent with the TCPP amount, as already shown with TGA and CHNS (Table S1, ESI†).

Effect of NP functionalization on the optical properties

The optical properties of functionalized nanosystems and single material components are analysed by both photo - (PL) and radioluminescence (RL) techniques to study the occurrence of optical interactions between the NPs and the dye, and their mechanisms radiative and non-radiative energy transfer are mainly investigated by PL and time resolved photoluminescence (TRPL) measurements, whereas the effect of density enhancement in proximity of the dye is investigated by RL.

The luminescence features of ZS-AP-0.1 and ZS-AP-1 and the component materials TCPP, ZS and ZS-A, detected under light excitation, are shown in Fig. 4(a) and (b). The optical properties of TCPP are in agreement with the literature,[57,59] and they are displayed in the top panel of Fig. 4(a): namely, the PL of TCPP shows two peaks centred at about 1.9 eV, related to the *Q*(0,0) transition from the dye monomer,[33] and at 1.7 eV, related to the *Q*(0,1) transition, known as J-bands, also associated with J-aggregate formation;[60] the PLE spectrum matches the absorption features, described in the

previous section (Fig. S7, ESI†). It is worth noticing that, at energies above the Soret band, the PLE intensity of the dye is not null (Fig. 4(a), the inset at the top) probably because of the presence of aggregates, especially dimers and trimers, which introduce additional absorption components.[42,44]

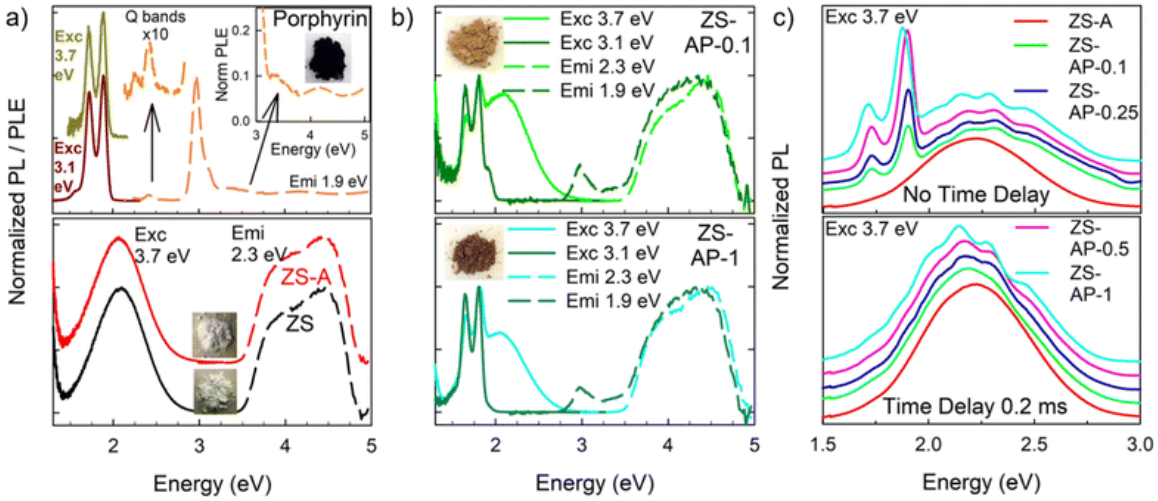

Fig. 4 *(a) and (b) Normalized steady-state PL (solid lines) and PLE (dashed lines) spectra obtained under CW excitation of (a) TCPP (top), ZS and ZS-A (bottom), and (b) ZS-AP-0.1 (top) and ZS-AP-1 (bottom), dispersed in DMF solution. In panel (a), enlargements of TCPP PLE between 2.2 and 2.8 eV (Q bands) and between 3.0 and 5.0 eV are also shown. Insets are digital pictures of the as-synthesized materials. (c) Normalized PL spectra of ZS-A and ZS-AP-Y dispersed in DMF solution and obtained simultaneously (top) and with 0.2 ms delay (bottom) with respect to an excitation pulse of 3.7 eV.*

The bottom panel of Fig. 4(a) shows the luminescence features of ZS and ZS-A. As unveiled in our previous works, all the ZS luminescence features from 1.7 to 3 eV, both under light and X-ray excitations, are attributable to defects in ZnO:[36,61] the SiO_2 substrate does not display any PL emission, while it shows a weak RL at 4 eV. No differences are observed between the optical properties of ZS and ZS-A, suggesting that the APTES anchoring does not alter ZnO luminescence, and it does not introduce any additional emission. The ZS bare NP broad defect-related PL is centred at about 2.2 eV with a corresponding PLE spectrum ranging from 3.5 to 5 eV.[36,61] The results obtained on the single components show that the ZnO emission is resonant with the TCPP Q-bands, indicating that the NP functionalization with the dye might permit both non-radiative and radiative energy transfers.[39]

In the following, the optical interaction between TCPP and ZS is verified and the luminescence mechanisms unveiled. All ZS-AP-Y samples display similar optical properties (Fig. 4(b) and Fig. S8, ESI†). In particular, the ZnO emission at 2.3 eV in ZS-AP-Y displays a PLE spectrum similar to the one of ZS, dominated by the ZnO absorption; besides, the PLE spectra monitored at 1.9 eV present the typical TCPP Soret band at 3 eV and ZnO PLE features at higher energies. On the other hand, the PL spectra of ZS-AP-Y obtained by exciting at 3.7 eV (in the absorption region of ZnO) reveal the presence of both ZnO broad bands and the TCPP red emission. These results indicate the presence of a double mechanism responsible for TCPP luminescence in functionalized NPs. In fact, since TCPP can be excited at energies higher than 3 eV, absorption by both ZnO and TCPP itself can generate

the corresponding yellow-green and red luminescence bands; on the other hand, the transfer of the excitation energy from ZnO to TCPP cannot be excluded.

By exciting ZS-AP-Y samples in the TCPP Soret band (at 3.1 eV), only the dye PLs at about 1.7 eV and 1.9 eV are observed; moreover, in addition to the characteristic TCPP PL features, a peak centred at about 2.0 eV is detected, especially in the samples with the lowest dye loading (ZS-AP-0.1 and ZS-AP-0.25). This band can be associated with the presence of Zn–TCPP complexes,[62,63] whose formation is due to the partial release of zinc ions from the highly reactive surface of ZnO NPs and their subsequent coordination with the porphyrin ring.[59]

An accurate discussion of data presented in Fig. 4(c) will be proposed later in the text.

TRPL measurements, as shown in Fig. 5, were performed to further investigate the occurrence of energy transfer processes between the NPs and TCPP. The time decays of the ZnO emissions of ZS, ZS-A and ZS-AP-Y (Fig. 5(a)–(c)), fitted with three-exponential functions with similar times and relative weight parameters (Table S4, ESI†), reveal the presence of slow components up to thousands of nanoseconds, as already highlighted by our previous study.[64] These findings unveil that the ZnO time dynamics does not vary among the samples, indicating the absence of Förster energy transfer between the dye and the NPs in the coupled nanomaterials. Probably, the TCPP spatial distribution with respect to ZnO in this material is not optimized to promote the non-radiative energy transfer mechanism. PL decays of TCPP emissions (Fig. (5)–(f) and Table S5, ESI†) display in all the samples the dye characteristic time decay component of about 11 ns, in agreement with the literature,[63,65] while only in ZS-AP-Y an additional fast component, whose relative weight is the highest regardless of the porphyrin content, of about 2.5 ns is detected.

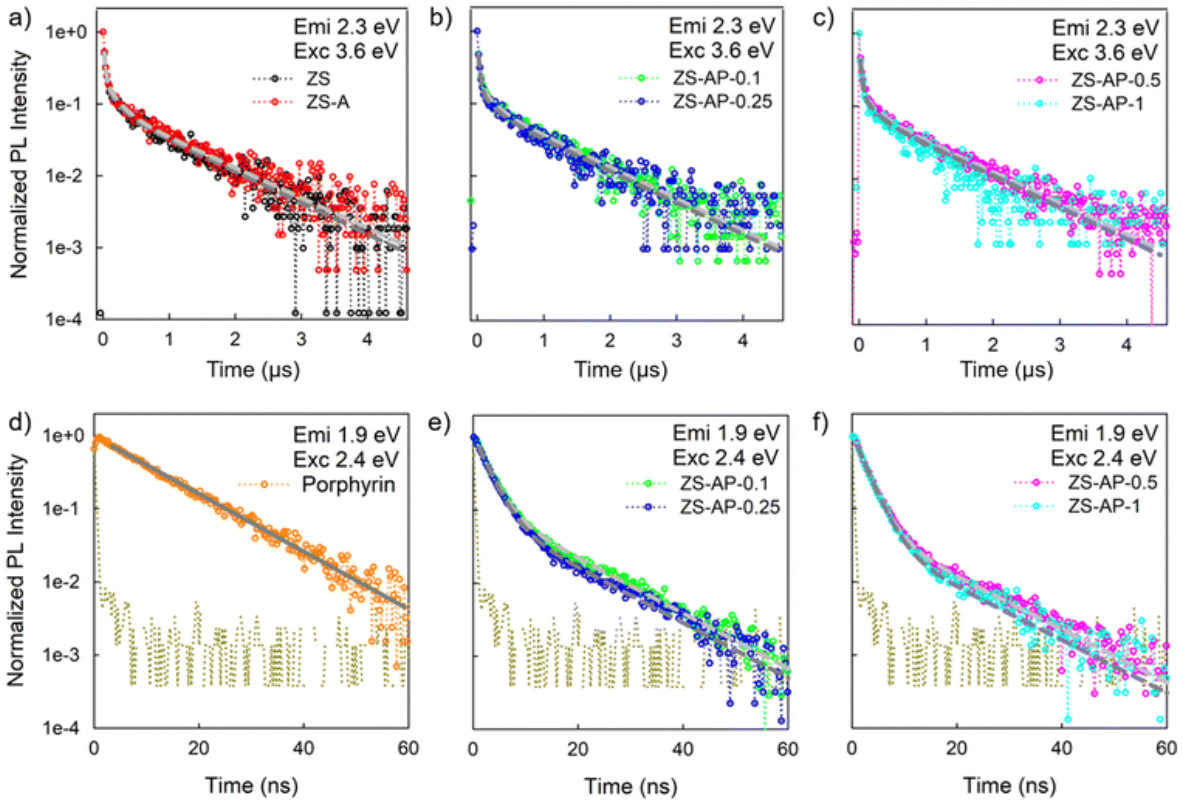

Fig. 5 *TRPL of the (a)–(c) ZnO emission obtained at 2.3 eV under pulsed excitation at 3.6 eV and (d) and (e) TCPP emission obtained at 1.9 eV under pulsed excitation at 2.4 eV for all the materials.*

The time decays are fitted as single (d) or multiexponential (a), (b), (c), (e), and (f) functions (solid lines). For (d)–(f), the instrument response function (IRF) is also shown (mustard dotted line). The complete set of parameters used to model the PL decay is reported in Tables S4 and S5 in the ESI.†

The origin of this fast component may be attributed to Zn–TCPP complexes, with an emission band at 2.0 eV (Fig. 4(b)) and with a time decay of about 2 ns as reported in the literature;[63,66] alternatively, it may be due to aggregate species. Usually, J-aggregates accelerate the characteristic porphyrin time dynamics,[58] whereas H-aggregates display bi-exponential behaviour with both very fast (about 2 ns) and longer (about 10 ns) decay times.[42] A conclusive attribution of the observed fast components results tricky, but in general its occurrence unveils the presence of dye complexes and/or aggregates.[19,42,44] For all the exponential PL decays, the complete data set of the obtained decay components with corresponding weights is reported in Tables S4 and S5 in the ESI.† These data reveal that, whatever is the origin of the fast luminescence, it dominates the luminescence of the porphyrin functionalized systems, with a weight of 80% over the total luminescence in ZS-AP-1, where the maximum creation of aggregates can occur.

Taking into consideration the very different order of magnitude of ZnO and dye luminescence lifetimes, the PL spectra of ZS-A and ZS-AP-Y obtained with 0 ms (no delay) and 0.2 ms time delays with respect to an excitation pulse of 3.7 eV (Fig. 4(c)) can be appropriately analysed. For all ZS-AP-Y samples, the ZnO emission shows dips, whose magnitude scales with the loading level, at energies (~2 eV, ~2.2 eV, and ~2.4 eV) matching the dye Q-bands, thus disclosing the occurrence of the TCPP re-absorption of the photons emitted by ZnO. A slight red shift of both porphyrin bands and dips in ZnO luminescence is observed in ZS-AP-1, possibly caused by the presence of a minor fraction of J-aggregates.[43] In this case, the experimental setup required the use of cuvettes of 1 cm, instead of 0.1 cm as previously used for registering PL and PL excitation (PLE) spectra in Fig. 4(a) and (b). Consequently, lengthening the light path (from 0.1 to 1 cm), hence emitted photons path, the probability of re-absorption increases. The dye emission intensity is strong when the signal is collected without delay (Fig. 4(c) in the top panel); by introducing a 0.2 ms delay, the dye luminescence is very weak (Fig. 4(c) in the bottom panel). To check the presence of the porphyrin bands in the PL spectra obtained with a 0.2 ms time delay after the lamp shutdown, first derivates of ZS-AP-Y signals are also computed and compared to those of ZS-A and TCPP (Fig. S9, ESI†): a relative minimum at 1.75 eV, which is clearly distinguishable in the TCPP spectrum, is also present in ZS-AP-Y, proving the occurrence of a weak dye luminescence. These results indicate that in ZS-AP-Y, during the excitation at 3.7 eV, both the NPs and TCPP are directly and continuously excited by UV light (Fig. 4(c) in the top panel); when the excitation source is switched off and the luminescence is collected after 0.2 ms, the porphyrin emission is produced only by the absorption of photons emitted by ZnO, being the dye decay time shorter (in the ns range) than the time delay used in the measurements. The evidence that the porphyrin luminescence intensity is weak in the spectra obtained with a 0.2 ms time delay (Fig. 4(c) in the bottom panel) unveils that the efficiency of radiative ET is rather poor.

To sum up, the main interaction mechanism under light excitation is a radiative phenomenon in which ZnO emitted photons are re-absorbed by porphyrin. Hence, an optical interaction between NPs and the dye in the nanoscintillators is only weakly achieved upon functionalization.

The normalized RL spectra obtained under X-ray irradiation of the single components and ZS-AP-Y are reported in Fig. 6(a) and (b). In addition, a mechanical mix (ZS-A + P-0.5), realized by stirring the APTES grafted bare nanoscintillator and TCPP with a loading level of 1.4 wt% is investigated, allowing the RL properties of two samples to be compared (namely ZS-AP-0.5 and ZS-A + P-0.5), which present the same porphyrin concentration, but the different spatial distribution. In fact, the mean inter-distance between ZnO NPs and TCPP in ZS-AP-Y probably ranges from few to tens of nanometers thanks to the bonding through APTES anchors, whereas it is increased from nano- to micro-meters in ZS-A + P-0.5, where the porphyrin is randomly distributed in the surroundings of ZS.

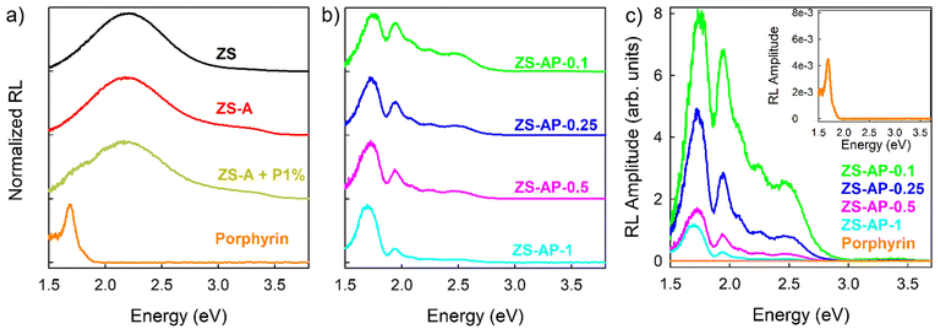

Fig. 6 *(a) and (b) Normalized RL spectra obtained under X-ray excitation of ZS, ZS-A, and TCPP and the mechanical mix of ZS-A + P-0.5 (a) and ZS-AP-Y (b). (c) RL intensities of ZS-AP-Y and TCPP normalized to their dye content. The inset is an enlargement of the TCPP spectrum.*

The RL spectra of ZS and ZS-A + P-0.25, in which the porphyrin luminescence is barely observed, are dominated by the broad ZnO defect-related emission, while that of the dye alone displays only the porphyrin band at 1.7 eV, in accordance with the aggregation of dye molecule powders on which measurements are performed (Fig. 6(a)). In ZS-AP-Y, the ZnO emission intensity scales coherently with the TCPP loading and its spectral shape is affected by the presence of dips at 2.2 and 2.4 eV (Fig. 6(b)), confirming the occurrence of the re-absorption mechanism even under irradiation with ionizing radiation. In all ZS-AP-Y samples, the characteristic porphyrin spectral components (at about 1.7 eV and at 1.9 eV), whose relative ratio increases as the dye loading level increases due to the higher probability of J-aggregate formation,[43] and the Zn–TCPP complexes band at about 2.0 eV, are distinguishable (Fig. 6(b)). Hence, the porphyrin luminescence is efficiently sensitized in all the functionalized nanomaterials regardless of the porphyrin content, with much greater evidence than in the ZS-AP-0.5 mechanical mix, in which the dye loading is of 1.4%. These findings disclose that functionalization allows in controlling the dye arrangement and spatial distribution and it is thus pivotal for the interaction between the single components in the coupled nanomaterials.

In Fig. 6(c), the dye and ZS-AP-Y RL intensities, normalized to the porphyrin content of the sample, are reported to highlight the effect of the high density nanoscintillators presence in the proximity of the dye upon their interaction under ionizing radiations. The RL of TCPP alone is of three orders of magnitude less intense in the dye than that in ZS-AP-Y, even if their porphyrin content (from 0.1% to 1%) is two/three orders of magnitude smaller than that in the dye alone (100%). These results point out that the interaction between ionizing radiations and organic molecules is poor because of their low density and low *Z* atomic number,[17] while the activation of

their luminescence is promoted by their proximity to heavy nanoscintillators,[13] which favours energy deposition in the dye surroundings. In the studied nanosystems, the X-ray photon energy can be deposited both in ZnO and SiO_2 NPs. In fact, the probability of interaction between the matter and ionizing radiation depends on atomic numbers (Z_{Zn} = 30, Z_{Si} = 14, Z_O = 8), densities (ρ_{ZnO} = 5.61 g cm^{-3}, Z_{SiO_2} = 2.65 g cm^{-3}), and particle dimensions (r_{Zn} = 2.5 nm, r_{Si} = 40 nm). As a preliminary evaluation of the role of SiO_2 and ZnO in the sensitization of the dye emission under ionizing radiation excitation, the RL spectra of only SiO_2 NPs coupled with 0.1 and 1 wt% of the dye were also recorded (Fig. S10, ESI†). The numerical analysis of the RL emissions discloses that the porphyrin luminescence is higher in the samples with ZnO NPs with respect to those made by SiO_2 alone (Fig. S11 and Table S3, ESI†). These data suggest that the heavy and scintillating ZnO NPs have a key role in promoting the dye emission. Nevertheless, the overall RL intensity decreases with the TCPP loading throughout the coupled nanomaterials, suggesting that upon functionalization new non-radiative dissipation channels are generated. Hence, the RL data indicate that the porphyrin emission enhancement in ZS-AP-Y is generated by both the re-absorption of ZnO emitted photons and the increased energy deposition of ionizing radiation in the porphyrin surroundings; remarkably, the efficiency of the two mechanisms depends on the dye arrangement and NP spatial distribution.

The results of the investigation reveal the achievement of hybrid nanoscintillators of ZnO/SiO_2 coupled with porphyrin with attractive properties for biomedical and oncological therapy applications. The attainment of the surface functionalization through APTES linkage was exploited to trigger the sensitization of the PL by ET and, especially, by energy deposition mechanisms under X-ray excitation. Nevertheless, the depicted scenario evidences the demand for further in-depth investigations to optimize the dye anchoring strategy on the ZnO/SiO_2 surface, to reduce the dye aggregates even at low photosensitizer loading and drive the ET, luminescence, and energy deposition mechanisms. This would lead to an increase of the dye cytotoxicity. An improved activation of the therapeutic action of the dye will represent a step forward towards the foreseen possible X-PDT application of these hybrid nanosystems.

Experimental

Materials

For ZnO/SiO_2 NP (ZS) synthesis, tetraethyl orthosilicate (TEOS, ≥99.0%), sodium hydroxide (≥98.0%), ammonium hydroxide solution (NH_4OH, 28 wt%), hexadecyltrimethylammonium bromide (CTAB, 98%) and zinc acetate dihydrate (>98%) were purchased from Merck Life Science (Merck KGaA, Darmstadt, Germany). For the functionalization with porphyrin, (3-aminopropyl)triethoxysilane ($H_2N(CH_2)_3Si(OC_2H_5)_3$, APTES, 98%), *N*,*N*-dimethylformamide (DMF, 99%) and toluene (99%) were purchased from Alfa Aesar; 5,10,15,20-(tetra-4-carboxyphenyl) porphyrin (TCPP, 98%) was used as received from PorphyChem SAS.

Synthetic procedures

The synthesis of TCPP functionalized ZnO/SiO_2 NPs was performed in four subsequent steps as shown in Fig. 1.

Synthesis of ZnO/SiO_2 NPs.A two-step reaction was carried out to prepare ZnO/SiO_2 NPs (ZS), as previously reported in ref. 64. SiO_2 NPs were first synthesized through a sol–gel method, using CTAB templating agent for controlling the growth of highly porous NPs according to ref. 67 (step I). Then, ZnO NPs were grown on the surface of SiO_2 NPs by hydrolysis and condensation of zinc acetate dihydrate[46,68] in ethanol under basic conditions (NaOH) (step II, ZnO nominal loading of 12.0 wt%, reaction yield ~80%).

Functionalization of ZS NPs with porphyrin.TCPP was covalently supported onto ZS by the reaction of the –COOH groups of TCPP with the amino groups of APTES used as the surface functionalizing agent. In detail, 2.0 g of ZS was dispersed in 48 mL of toluene at 120 °C; then, 16 µL of APTES was added and the reaction was left under stirring for 24 h under reflux (step III). Then the powders were filtrated, washed twice with fresh toluene, and dried overnight at 100 °C. Hereafter, this sample was labelled as ZS-A. In the last step, different TCPP amounts were loaded onto ZS-A (step IV). 0.5 g of ZS-A was dispersed in 25 mL of DMF at room temperature and different amounts of TCPP were added (APTES : TCPP molar ratios equal to 1 : 1, 1 : 0.5, 1 : 0.25, and 1 : 0.1 corresponding to a dye loading equal to 2.7, 1.4, 0.7, and 0.3 wt%, respectively). After 18 h, the products were isolated by centrifugation, washed twice with fresh DMF and dried overnight at 80 °C. TCPP functionalized SiO_2 NPs will be labelled as ZS-AP-Y, where Y is the APTES : TCPP molar ratio used during synthesis.

Mechanical mix.A homogenous mechanical mix of 98.6 mg of bare ZS-A with 1.4 mg of TCPP (TCPP amount equal to 1.4 wt%) was prepared as the comparison material to further investigate the role of TCPP–ZnO proximity on the luminescence properties. This sample was labelled as ZS-A + P-0.5.

Structural and morphological characterization

The morphological analysis was carried out on all samples by TEM. TEM images were collected using a JEOL JEM-2100Plus TEM (JEOL, Akishima, Tokio, Japan) operating with an acceleration voltage of 200 kV, equipped with an 8-megapixel Gatan (Gatan, Pleasanton, CA, USA) Rio™ complementary metal-oxide-semiconductor (CMOS) camera. The samples were deposited onto carbon coated Cu TEM mesh grids by drop-casting dilute NP dispersions in ethanol. The sizes of SiO_2 and ZnO NPs were determined by manually measuring 100 particles randomly chosen. To obtain insights into ZnO NP distribution at the different reaction stages, elemental mapping was performed using an energy dispersive X-ray spectrometer (EDS)-equipped TEM.

The porosity of SiO_2 NPs was studied by nitrogen physisorption using a Micromeritics ASAP 2020 HD analyser, after degassing the samples at 100 °C under vacuum. SSA values, desorption cumulative pore volume (DCPV) and pore size distribution were obtained using the Brunauer–Emmett–Teller (BET) model.

The formation of ZnO NPs in ZS through step II was confirmed by DRS, by measuring the reflectance percentage (R%) in the range of 400–300 nm. The instrument used was a Lambda 900 PerkinElmer UV spectrometer.

The structural features were investigated by XRPD, using a Rigaku MiniFlex 600 diffractometer with 0.154 nm Cu Kα radiation (Rigaku Corporation, Akishima-Shi, Tokyo, Japan). The measurements were performed in the 2ϑ range of 20–70° (2ϑ step 0.02°, 1° min^{-1} scan rate).

Raman spectroscopy was performed to validate the nature of the oxides and their interaction in the ZS sample. Raman spectroscopy was performed using a LabRam (Jobin Yvon, France) spectrometer equipped with a BX40 microscope head (Olympus, Japan) and focusing a helium–neon laser working at 633 nm with a long working distance 50× objective with a numerical aperture of 0.60.

The functionalization with both APTES and TCPP was qualitatively studied by FTIR-ATR by using a Thermo Fisher Scientific Nicolet iS20, wavenumber range between 4000 and 550 cm^{-1}, resolution spectra 4 cm^{-1}, 32 scans. The amount of the organic substituents was quantified by TGA using a Mettler Toledo TGA/DSC1 STAR e System (30–1000 °C, a heating rate of 10 °C min^{-1}, and a constant air flux of 50 mL min^{-1}) and further confirmed by elemental analysis (CHNS), performed using an Elemental VarioMICRO analyser (temperature of the combustion column = 1150 °C, reduction column = 850 °C). From the thermal profiles measured during TGA, the weight loss between 150 and 1000 °C ($\Delta W_{150–1000\ °C}$) was used to calculate (i) the amounts of APTES and TCPP in ZS-A and ZS-AP-Y samples (TCPP amount, wt%), respectively, and (ii) the ratio between APTES and TCPP molecules distributed over the SiO_2 surface (number of molecules per nm^2 SiO_2), according to eqn (S1)–(S3) in the ESI.†

Spectroscopic characterization

Absorption spectra from 200 to 800 nm were recorded using a double beam PerkinElmer Lambda 950 spectrometer with a spectral resolution of 1.0 nm using Suprasil quartz cuvettes with a 0.1 cm optical path length. A calibration curve was obtained by measuring the absorption spectra of TCPP solution in DMF at known concentrations (in the range: 10^{-6}–7×10^{-5} M, data not shown) by monitoring the TCPP absorbance at 520 nm corresponding to the first peak of the Q bands (Abs_{520}). In this concentration range, Abs_{520} has a linear increase with the TCPP concentration. The TCPP amount in ZS-AP-Y was calculated by using the Lamber Beer equation (eqn (S4), ESI†).

Excitation–emission luminescence measurements were carried out in the steady-state mode exciting using a continuous wave (CW) Xenon lamp coupled to a double monochromator (Jobin-Yvon Gemini 180 with 1200 grooves per mm gratings), and recording through a nitrogen cooled, back illuminated, UV enhanced, Charge-Coupled Device (CCD) detector coupled to a monochromator (Jobin-Yvon Micro HR with a 150 grooves per mm grating). PL spectra were recorded exciting at ~335 nm (~3.7 eV) for all the samples and at ~400 nm (~3.1 eV) only for TCPP and ZS-AP-Y samples. PLE spectra were detected monitoring the TCPP emission at ~655 nm (~1.9 eV) for TCPP and ZS-AP-Y samples; the ZnO emission at ~540 nm (~2.3 eV) for ZS, ZS-A and ZS-AP-Y samples. All the spectra were corrected for the spectral response of the system.

TRPL measurements were carried out in the time correlated single photon counting (TCSPC) mode using a FLS 980 spectrofluorometer by Edinburgh Photonics using Suprasil quartz cuvettes with a 0.1 cm optical path length. TRPL spectra monitored at 2.3 eV (540 nm) with a band-width of 10 nm were recorded using a pulsed diode light emitting device (EPLED) emitting at 3.6 eV (340 nm)

as the excitation source with a pulse width of ∼950 ps; the TRPL decays of TCPP and ZS-AP-Y monitored at 1.9 eV (650 nm) with a bandwidth of 5 nm were obtained exploiting a pulsed diode laser (EPL) emitting at 2.4 eV (510 nm) with a pulse width of ∼280 ps.

Finally, time resolved emission spectroscopy (TRES) was also applied: the emission spectra were recorded both immediately after the pulse and with 0.2 ms delay exciting at 340 nm with a Xenon flash lamp with a pulse duration of 0.1 ms using an Agilent Cary Eclipse fluorimeter using Suprasil quartz cuvettes of 1 cm optical path length. For all the samples, measurements were performed at room temperature and atmospheric pressure in DMF solutions.

Steady state RL measurements were carried out using a homemade apparatus featuring, as a detection system, a CCD Jobin-Yvon Symphony II coupled with a spectrograph Jobin-Yvon Triax 180 operating in the range of 200–1100 nm. All the spectra were collected on sample powders at room temperature and at a pressure of 10^{-3} mbar to avoid any RL emission from molecules present in the air and corrected for the spectral response of the detection system. RL excitation was obtained by X-ray irradiation through a Be window, using a Philips 2274 X-ray tube with a tungsten target operating at 20 kV and 20 mA. At the used voltage, the continuous X-ray spectrum, with a mean energy of 6–7 keV, is produced mainly by a bremsstrahlung mechanism superimposed to the L and M transitions of tungsten.[69]

Conclusions

In this work, we propose a reliable approach towards the designing of efficient hybrid NPs. We based the realization of this methodology on a specific case of study involving scintillating ZnO NPs supported on silica with TCPP porphyrins at different loadings, with the future aim to engineer a material suitable for X-PDT application.

This study presents an exploration of the structural, morphological, and luminescence properties of the components of the hybrid nanosystem taken individually and assembled in the final architecture, with particular interest in the role played by the material mesoporosity and the mean inter-distance between the nanoscintillators and the dyes, also in the presence of ionizing radiations. Importantly, the photoluminescence measurements on the dye functionalized ZnO NPs unveil the formation of porphyrin aggregates depending on the dye concentration, and the absence of Förster energy transfer. Under light excitation, the porphyrin emission is mainly due to the re-absorption of ZnO emitted photons; in contrast, dye sensitization is boosted upon X-ray irradiation thanks to augmented energy deposition in proximity of the dense inorganic NPs. These findings suggest that the mutual dye spatial distribution and their arrangement on the NP surface determined by the loading strategy are crucial parameters for the activation of the organic dye luminescence and thus of its cancer killing activity. This study highlights the synergic contribution of the functionalization strategy and ionizing radiation on the interactions between nanoscintillators and organic fluorescent molecules, indicating the critical aspects of the structure of the material which affect the resultant luminescence performances of multicomponent systems in diverse applications, such as in X-PDT.

The findings of this work prove the cruciality of the development of a robust methodology to explore the properties of the hybrid NP and they pave the way for further investigating the X-ray

induced mechanisms (both radiative transfer and locally augmented energy deposition, respectively) by experimental and computational approaches to optimize the design of hybrid nanomaterials with tailored performances for specific applications and technologies.

Author contributions

Conceptualization: I. V., S. M., M. D. A., B. D. C., R. S. and A. V.; formal analysis: R. C.; investigation: R. C. R. L. and S. M.; supervision: I. V., R. S., and A. V.; validation: S. M., M. D. A., B. D. C., M. F., R. L., R. S. and A. V.; visualization: R. C.; writing – original draft: R. C. and S. M.; writing – review and editing: I. V. All the authors have read and agreed to the published version of the manuscript. R. C. and S. M. contributed equally to this study.

Conflicts of interest

There are no conflicts to declare.

Acknowledgements

This work was supported by the Skłodowska-Curie Actions Widening Fellowship (MSCA-WF): NUMBER 101003405—HANSOME.

References

1. T. Sun, Y. S. Zhang, B. Pang, D. C. Hyun, M. Yang and Y. Xia, *Angew. Chem., Int. Ed.*, 2014, **53**, 12320
2. I. Villa, F. Moretti, M. Fasoli, A. Rossi, B. Hattendorf, C. Dujardin, M. Niederberger, A. Vedda and A. Lauria, *Adv. Opt. Mater.*, 2020, **8**, 1901348
3. S. Mostoni, P. Milana, B. Di Credico, M. D'Arienzo and R. Scotti, *Catalysts*, 2019, **9**, 664
4. S. Goel, D. Ni and W. Cai, *ACS Nano*, 2017, **11**, 5233–5237
5. K. Tanaka and Y. Chujo, *Adv. Powder Technol.*, 2014, **25**, 101–113
6. R. Mout, D. F. Moyano, S. Rana and V. M. Rotello, *Chem. Soc. Rev.*, 2012, **41**, 2539
7. C. Xu, P. Ravi Anusuyadevi, C. Aymonier, R. Luque and S. Marre, *Chem. Soc. Rev.*, 2019, **48**, 3868–3902
8. V. P. Ananikov, *Nanomaterials*, 2019, **9**, 1197
9. T. Sen and I. J. Bruce, *Sci. Rep.*, 2012, **2**, 564
10. M. Gandini, I. Villa, M. Beretta, C. Gotti, M. Imran, F. Carulli, E. Fantuzzi, M. Sassi, M. Zaffalon, C. Brofferio, L. Manna, L. Beverina, A. Vedda, M. Fasoli, L. Gironi and S. Brovelli, *Nat. Nanotechnol.*, 2020, **15**, 462–468
11. U. Szeluga, B. Kumanek and B. Trzebicka, *Composites, Part A*, 2015, **73**, 204–231
12. W. Park, H. Shin, B. Choi, W.-K. Rhim, K. Na and D. Keun Han, *Prog. Mater. Sci.*, 2020, **114**, 100686

13. P. Juzenas, W. Chen, Y.-P. Sun, M. A. N. Coelho, R. Generalov, N. Generalova and I. L. Christensen, *Adv. Drug Delivery Rev.*, 2008, **60**, 1600–1614
14. L. Larue, A. Ben Mihoub, Z. Youssef, L. Colombeau, S. Acherar, J. C. André, P. Arnoux, F. Baros, M. Vermandel and C. Frochot, *Photochem. Photobiol. Sci.*, 2018, **17**, 1612–1650
15. X.-D. Ren, X.-Y. Hao, H.-C. Li, M.-R. Ke, B.-Y. Zheng and J.-D. Huang, *Drug Discovery Today*, 2018, **23**, 1791–1800
16. R. Crapanzano, V. Secchi and I. Villa, *Appl. Sci.*, 2021, **11**(15), 7073
17. G. F. Knoll, *Med. Phys.*, 1980, **7**, 397–398
18. S. Clement, J. M. Campbell, W. Deng, A. Guller, S. Nisar, G. Liu, B. C. Wilson and E. M. Goldys, *Adv. Sci.*, 2020, **7**, 2003584
19. I. Villa, C. Villa, R. Crapanzano, V. Secchi, M. Taw, E. Trombetta, L. Porretti, A. Brambilla, M. Campione, Y. Torrente, A. Vedda and A. Monguzzi, *ACS Appl. Mater Interfaces*, 2021, **13**(11), 12997
20. W. Sun, Z. Zhou, G. Pratx, X. Chen and H. Chen, *Theranostics*, 2020, **10**, 1296–1318
21. A.-L. Bulin, M. Broekgaarden, D. Simeone and T. Hasan, *Oncotarget*, 2019, **10**, 2625–2643
22. W. Park, H. Shin, B. Choi, W.-K. Rhim, K. Na and D. Keun Han, *Prog. Mater. Sci.*, 2020, **114**, 100686
23. M. J. Sailor and J.-H. Park, *Adv. Mater.*, 2012, **24**, 3779–3802
24. J. Perego, I. Villa, A. Pedrini, E. C. Padovani, R. Crapanzano, A. Vedda, C. Dujardin, C. X. Bezuidenhout, S. Bracco, P. E. Sozzani, A. Comotti, L. Gironi, M. Beretta, M. Salomoni, N. Kratochwil, S. Gundacker, E. Auffray, F. Meinardi and A. Monguzzi, *Nat. Photonics*, 2021, **15**, 393–400
25. C. Dujardin, E. Auffray, E. Bourret-Courchesne, P. Dorenbos, P. Lecoq, M. Nikl, A. N. Vasil'Ev, A. Yoshikawa and R. Y. Zhu, *IEEE Trans. Nucl. Sci.*, 2018, **65**, 1977–1997
26. A.-L. Bulin, A. Vasil'ev, A. Belsky, D. Amans, G. Ledoux and C. Dujardin, *Nanoscale*, 2015, **7**, 5744–5751
27. S. Incerti, M. Douglass, S. Penfold, S. Guatelli and E. Bezak, *Phys. Med.*, 2016, **32**, 1187–1200
28. S. S. Lucky, K. C. Soo and Y. Zhang, *Chem. Rev.*, 2015, **115**, 1990–2042
29. P. K. Mishra, H. Mishra, A. Ekielski, S. Talegaonkar and B. Vaidya, *Drug Discovery Today*, 2017, **22**, 1825–1834
30. R. Generalov, W. B. Kuan, W. Chen, S. Kristensen and P. Juzenas, *Colloids Surf., B*, 2015, **129**, 79–86
31. Y. Liu, Y. Zhang, S. Wang, C. Pope and W. Chen, *Appl. Phys. Lett.*, 2008, **92**, 143901
32. S. Sadjadpour, S. Safarian, S. J. Zargar and N. Sheibani, *Biotechnol. Appl. Biochem.*, 2016, **63**, 113–124
33. L. Procházková, I. T. Pelikánová, E. Mihóková, R. Dědic and V. Čuba, *Radiat. Meas.*, 2019, **121**, 13–17
34. Ü. Özgür, Y. I. Alivov, C. Liu, A. Teke, M. A. Reshchikov, S. Doğan, V. Avrutin, S. J. Cho and H. Mork, *J. Appl. Phys.*, 2005, **98**, 1–103
35. P. A. Rodnyi and I. V. Khodyuk, *Opt. Spectrosc.*, 2011, **111**, 776–785
36. R. Crapanzano, I. Villa, S. Mostoni, M. D'arienzo, B. Di Credico, M. Fasoli, R. Scotti and A. Vedda, *Nanomaterials*, 2020, **10**, 1–19

37. P. Camarda, F. Messina, L. Vaccaro, S. Agnello, G. Buscarino, R. Schneider, R. Popescu, D. Gerthsen, R. Lorenzi, F. M. Gelardi and M. Cannas, *Phys. Chem. Chem. Phys.*, 2016, **18**, 16237–16244
38. Z. Youssef, R. Vanderesse, L. Colombeau, F. Baros, T. Roques-Carmes, C. Frochot, H. Wahab, J. Toufaily, T. Hamieh, S. Acherar and A. M. Gazzali, *Cancer Nanotechnol.*, 2017, **8**, 6
39. J. R. Lakowicz, *Principles of fluorescence spectroscopy*, Springer, US, Boston, MA, 3th edn, 2006
40. G. De Luca, A. Romeo, V. Villari, N. Micali, I. Foltran, E. Foresti, I. G. Lesci, N. Roveri, T. Zuccheri and L. M. Scolaro, *J. Am. Chem. Soc.*, 2009, **131**, 6920–6921
41. J. L. Bricks, Y. L. Slominskii, I. D. Panas and A. P. Demchenko, *Methods Appl. Fluoresc.*, 2017, **6**(1), 012001
42. N. C. Maiti, S. Mazumdar and N. Periasamy, *J. Phys. Chem. B*, 1998, **102**, 1528–1538
43. A. Monguzzi, I. G. Lesci, G. C. Capitani, N. Santo, N. Roveri and M. Campione, *Phys. Chem. Chem. Phys.*, 2014, **16**, 2491–2498
44. R. F. Khairutdinov and N. Serpone, *J. Phys. Chem. B*, 1999, **103**, 761–769 .
45. N. Keller, M. Calik, D. Sharapa, H. R. Soni, P. M. Zehetmaier, S. Rager, F. Auras, A. C. Jakowetz, A. Görling, T. Clark and T. Bein, *J. Am. Chem. Soc.*, 2018, **140**, 16544–16552
46. A. Susanna, L. Armelao, E. Callone, S. Dirè, M. D'Arienzo, B. Di Credico, L. Giannini, T. Hanel, F. Morazzoni and R. Scotti, *Chem. Eng. J.*, 2015, **275**, 245–252
47. F. L. Galeener, *Phys. Rev. B: Condens. Matter Mater. Phys.*, 1978, **17**, 1928
48. A. E. Geissberger and F. L. Galeener, *Phys. Rev. B: Condens. Matter Mater. Phys.*, 1983, **28**, 3266–3271
49. C. A. Murray and T. J. Greytak, *Phys. Rev. B: Condens. Matter Mater. Phys.*, 1979, **20**, 3368
50. F. L. Galeener, *Solid State Commun.*, 1982, **44**(7), 1037
51. F. Cova, A. Benedetto, N. Chiodini, R. Lorenzi, A. Vedda and V. Ouspenski, *J. Non-Cryst. Solids*, 2021, **555**, 120534 .
52. G. Buscarino, V. Ardizzone, G. Vaccaro, S. Agnello and F. M. Gelardi, *J. Appl. Phys.*, 2010, **108**(7), 074314
53. M. Heili, B. Poumellec, E. Burov, C. Gonnet, C. le Losq, D. R. Neuville and M. Lancry, *J. Mater. Sci.*, 2016, **51**, 1659
54. A. I. D. Cano, B. el Filali, T. V. Torchynska and J. L. C. Espinola, *J. Phys. Chem. Solids*, 2013, **74**, 431
55. A. el Manouni, F. J. Manjón, M. Perales, M. Mollar, B. Marí, M. C. Lopez and J. R. Ramos Barrado, *Superlattices Microstruct.*, 2007, **42**(1–6), 134
56. S. Degioanni, A. M. Jurdyc, A. Cheap, B. Champagnon, F. Bessueille, J. Coulm, L. Bois and D. Vouagner, *J. Appl. Phys.*, 2015, **118**, 153103
57. P. G. Mahajan, N. C. Dige, B. D. Vanjare, A. R. Phull, S. J. Kim, S. K. Hong and K. H. Lee, *J. Fluoresc.*, 2018, **28**, 871–882
58. V. Villari, P. Mineo, E. Scamporrino and N. Micali, *RSC Adv.*, 2012, **2**, 12989–12998
59. W. Zhang and E. P. C. Lai, *AIMS Environ. Sci.*, 2018, **5**, 67–77
60. C. K. Hope, K. Billingsley, E. J. De De Jong and S. M. Higham, *PLoS One*, 2016, **11**(7), e0158835
61. A. B. Djurišić and Y. H. Leung, *Small*, 2006, **2**, 944–961

62. G. D. Pierini, V. H. A. Pinto, C. G. C. Maia, W. D. Fragoso, J. S. Reboucas, M. E. Centurión, M. F. Pistonesi and M. S. Di Nezio, *Luminescence*, 2017, **32**, 1227–1232
63. R. L. Brookfield, H. Ellul and A. Harriman, *J. Photochem.*, 1985, **31**, 97–103
64. M. D'Arienzo, S. Mostoni, R. Crapanzano, C. Cepek, B. Di Credico, M. Fasoli, S. Polizzi, A. Vedda, I. Villa and R. Scotti, *J. Phys. Chem. C*, 2019, **123**, 21651–21661
65. Z. Gao, F. Chen, Y. Li, Y. Zhang, K. Cheng, P. An and B. Sun, *Dalton Trans.*, 2019, **48**, 16861–16868
66. J. Liu, J. W. Huang, H. Shen, H. Wang, H. C. Yu and L. N. Ji, *Dyes Pigm.*, 2008, **77**, 374–379
67. R. Scotti, L. Conzatti, M. D'Arienzo, B. Di Credico, L. Giannini, T. Hanel, P. Stagnaro, A. Susanna, L. Tadiello and F. Morazzoni, *Polymer*, 2014, **55**, 1497–1506
68. A. Susanna, M. D'Arienzo, B. Di Credico, L. Giannini, T. Hanel, R. Grandori, F. Morazzoni, S. Mostoni, C. Santambrogio and R. Scotti, *Eur. Polym. J.*, 2017, **93**, 63–74
69. J. A. Bearden, *Rev. Mod. Phys.*, 1967, **39**, 78–124

† Electronic supplementary information (ESI) available. See DOI: https://doi.org/10.1039/d2cp00884j